This manuscript was accepted by Phys. Plasmas. Click here to see the version of record.

Electron density evolution during a fast, non-diffusive propagation of a magnetic field in a multi-ion-species plasma

R. Doron,[1] B. Rubinstein,[1] J. Citrin,[1, a)] R. Arad,[1, b)] Y. Maron,[1] A. Fruchtman,[2] H.R. Strauss,[3] and T. A. Mehlhorn[4]

[1)] *Weizmann Institute of Science, Rehovot 76100, Israel*

[2)] *H.I.T. - Holon Institute of Technology, Holon 58102, Israel*

[3)] *HRS Fusion, West Orange, NJ 07052, USA*

[4)] *Plasma Physics Division, Naval Research Laboratory, Washington D.C. 20375, USA*

(Dated: 22 November 2016)

We present spectroscopic measurements of the electron density evolution during the propagation of a magnetic-field front (peak magnitude $\sim 8\,\mathrm{kG}$) through low-resistivity, multi-ion species plasma. In the configuration studied, a pulsed current, generating the magnetic field, is driven through a plasma that pre-fills the volume between two electrodes. 3D, spatial resolution is achieved by local injection of dopants via an optimized laser blow-off technique. The electron density evolution is inferred from the intensity evolution of Mg II and B II-III dopants line-emission. The Doppler-shifted line-emission of the light boron that is accelerated by the magnetic field is also used to determine the electric-potential-hill associated with the propagating magnetic field. Utilizing the same spectral line for the determination of both the density and the electric potential allowed for exploring the precise correlation between these two key parameters. For these measurements, achieving a high spatial resolution (a small fraction of the magnetic-field front) was necessary. The density evolution is found to be consistent with a scenario in which ions with relatively high charge-to-mass ratios are reflected by different potential heights, namely, reflected off the magnetic-field front at different field magnitudes; whereas the plasma of ions with low charge-to-mass ratios is penetrated by the magnetic field.

[a)] Present address: FOM Institute DIFFER - Dutch Institute for Fundamental Energy Research.

[b)] Present address: Soreq Nuclear Research Center.

I. INTRODUCTION

A magnetic field interacting with plasma transfers momentum and energy to the plasma, resulting in heating and pushing of the plasma. The interaction is manifested by two competing processes, pushing of the plasma by magnetic pressure, and penetration of the magnetic field into the plasma. Pushing of the plasma is dominant when the penetration is slow due to a low plasma resistivity. A high-density current is induced between the plasma and the magnetic-field front, and the plasma is pushed by the $\mathbf{J} \times \mathbf{B}$ force to the hydromagnetic velocity, which is larger than the velocity of the magnetic field front. The hydrodynamic velocity varies between twice the magnetic front propagation velocity (specular reflection[1]) and about the magnetic field velocity (snowplow[2]). Fast magnetic field penetration occurs at the high resistivity limit, the current layer then broadens and the field penetrates into the plasma by diffusion. Magnetic field that penetrates rapidly also into a low-resistivity plasma has been observed, both in laboratory plasmas[3–8] and in space[9–12]. Theories explaining the magnetic field penetration in part of these cases are based on the Hall-field mechanism within the frame-work of the electron-magnetohydrodynamic (EMHD) model, in which a narrow current layer is expected to penetrate into the plasma while ions are nearly motionless[13–17].

The different forms of the magnetic field-plasma interactions give rise to different electron density evolutions. Thus, knowledge of the electron density is useful for studying this interaction. Due to the quasi-neutrality of the plasma and to the conservation of the electron fluid, plasma pushing is accompanied by a compression of the electron fluid. In the ideal low-resistivity picture, the plasma is reflected by the magnetic-field front and the electron density is expected to rise to twice its initial value over the scale of the electron skin depth in front of the current layer, and then drop to zero behind the propagating field front[1]. If there are collisions in the pushed plasma the density will rise due to the accumulating plasma in front of the propagating field front, often as a snowplow, as previously observed[18]. When the field penetration is fast, either by diffusion due to high resistivity, or by the Hall-field-induced mechanism, no significant electron density change is expected.

The possibility of a more complex plasma dynamics was suggested by early simulations[19–21] and models[22,23]. More recent simulations show that when electron inertia is considered turbulence effects may develop[24] and the current layer is expected to break into vortices[25–28] that may affect the velocity and nature of magnetic field penetration[28]. Laboratory observations in such systems of low-resistivity, *multi-ion-species* plasmas (mostly protons and carbon ions), revealed a phenomenon of simultaneous field penetration and plasma pushing[29]. In these experiments, the heavier-ion plasma component (carbon) is penetrated by the magnetic field at a rate much faster than expected from diffusion[30], whereas the light-ion plasma (protons) is reflected off the field front, acquiring velocities that are about

twice the magnetic-field front propagation velocity[31]. The ions in the plasma penetrated by the magnetic field are also found to acquire non-negligible velocities relative to the magnetic-field propagation velocity. This complex plasma dynamics, involving both magnetic field penetration and plasma pushing, should be manifested in the electron density evolution.

In the configuration studied, a pulsed current, generating a magnetic field, propagates in a plasma that pre-fills the region between two planar electrodes. Previous spectroscopic measurements of the electron density have shown a density rise of up to $\sim 50\%$, which generally accompanies the arrival of the magnetic field to the region of observation, followed by a sharp density drop[30]. This observation was consistent with earlier line-integrated density measurement in similar systems[32,33]. The spatially resolved spectroscopic measurements showed that part of the plasma is indeed penetrated by the magnetic field and remains behind the propagating field front. The rise in the density was mainly attributed to the effect of the proton-plasma reflection. The subsequent density drop also seemed to be consistent with this reflection. However, a quantitative analysis showed that the proton reflection cannot account for the entire observed density drop[30].

Here, using the same multi-ion species system used in Ref.[30], we employ spectroscopic techniques with significantly improved spatial resolution to study in detail the electron density evolution during the plasma-magnetic field interaction. Furthermore, Doppler shifts of the same line emission that is utilized for the density measurements, are also utilized for the determination of the electric potential (referred to as potential hill) that develops due to the magnetic-field propagation. This allows for exploring the correlation between the density and the potential hill evolutions. This is otherwise very difficult to investigate due to unavoidable irreproducibilities in the system that make it nearly impossible to correlate parameters obtained in separate discharges.

We achieve a mm-scale spatial resolution, which is a few times the electron skin depth of our system that is the lowest expected current-layer width. The improved resolution reveals a significantly higher electron density rise, followed by a sharp drop to $\sim 10\%$ of the peak electron density. The measured potential hill is used to infer the ion dynamics that are found to be consistent with the density evolution. We conclude that the reflection of the relatively highly-charged carbon ions (C IV-V) plays a major role in the density evolution, particularly in forming the sharp density peak that was previously mainly attributed to the proton reflection.

II. THE EXPERIMENTAL SYSTEM

The experiment, schematically described in Fig. 1, consists of filling up the volume between two planar electrodes with plasma, followed by driving a pulsed current between

ing electrodes that rises to 130 kA in $\sim$ 350 ns. This produces the magnetic field (peak magnitude $\sim$ 8 kG) that interacts with the prefilled plasma. For the coordinates defined in Fig. 1: $x = 0$ is the cathode surface, $y = 0$ is the center of the electrodes, and $z = 0$ is the generator side edge of the prefilled plasma. The magnetic field propagates from the generator side in the z direction, towards a shorted end. The plasma is produced by two surface-flash-over plasma sources (flashboard), mounted outside the interelectrode gap, a few cm above a transparent wire-anode. The plasma expansion forms a density gradient across the anode-cathode (A-K) gap that supports Hall-field induced penetration. The electrodes are 14-cm wide (in the y direction), 8-cm long (along z) and separated by a 2.5-cm gap (along x). Each of the electrodes is an array of eight 1-mm-diameter wires with a geometric transparency of 93%, allowing for a nearly free flow of the plasma. The flashboard plasma is dominated by protons and carbon ions (mainly C III-V). The current generating the magnetic field is applied 1.1 μs after the application of the flashboard plasma source. By this time, the electron density (n_e) and temperature (T_e) in the middle of the interelectrode gap are found to be[34], respectively, $n_e \sim 3 \times 10^{14}$ cm^{-3} and $T_e \sim 6.5$ eV.

Radiation emitted from the plasma is imaged on a 1-m spectrometer input slit. The spectrometer output is conveyed to an array of fast photo-multipliers (PMTs) via a bundle of optical fibers. The spectral resolution varies from 0.07 to 0.12 Å over the spectral region recorded (2000 $-$ 7000 Å). The PMTs have a rise time of less than 3 ns and an exponential decay with a time constant of 6 ns. A second 0.25-m imaging spectrometer is coupled to a gated (7-ns) intensified charge-coupled device (ICCD) camera. The data recorded with the imaging spectrometer are mainly used for characterizing the geometry of the dopant columns injected into the plasma.

3-D spatially resolved measurements are obtained using a controlled injection of selected dopants into the plasma. In this approach, the plasma is doped by an atomic or ionic beam, the line emission of which is distinguished from the ambient plasma and can be used for diagnosing the local plasma parameters. In the present study, lines of B II-III and Mg II dopants are used. A laser blow-off technique[35–37] is used to inject the dopants into the plasma. The dopant is blown off a coated slide by a pulsed laser beam (doubled Nd-YAG, 160 mJ per 5 ns), hitting the slide from its uncoated side. An iris positioned between the slide and the prefilled plasma serves to collimate the plume. Plumes of a diameter smaller than 5 mm (containing 80% of the ions) for boron, and about 2 mm for magnesium, were obtained by optimizing the system parameters. The dopant plume was injected into the plasma in the x-direction from the cathode side ($x = 0$) prior to the injection of the plasma. The dopant-ion densities were found to be $\sim 2 \times 10^{13}$ cm^{-3} (determined spectroscopically), contributing less than 10% of the total electron density, ensuring minimal perturbation of the ambient plasma. The velocity (along the x-axis) of the dopant plume is $v_d \sim 6 \times 10^5$ cm/sec,

This manuscript was accepted by Phys. Plasmas. Click here to see the version of record.

approximately 10% of the velocity of the plasma injected into the inter-electrode gap.

The density observations were carried out along the y-axis (perpendicular to the field propagation direction). The data was collected from a region close to the center of the inter-electrode gap: at $x = 10\,\text{mm}$, $y = 0\,\text{mm}$, and $z = 37\,\text{mm}$. To optimize the light collection efficiency, a lens was placed inside the vacuum chamber, as close as possible to the dopant plume. The resolutions achieved in the x and z directions were 0.1 mm and 0.8 mm re axis y), determine

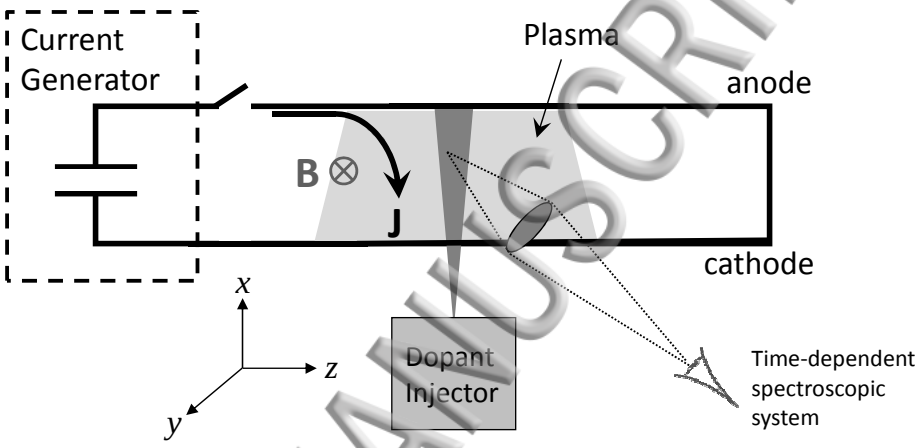

FIG. 1. A schematic desctiption of the experimental system. The generated magnetic field is directed along the y axis and propagates in the z direction.

III. ELECTRON DENSITY EVOLUTION

The evolution of the electron density was obtained from the evolution of line emission of B II, B III, and Mg II dopants. The time-dependent emission line intensities were used to yield the electron density and temperature evolution using collisional radiative (CR) modeling[38]. The analysis was performed in two stages. In the first stage, we determined the plasma parameters prior to the application of the pulsed magnetic field, utilizing Mg II line emission. Since the sensitivity of the Mg II-based density diagnostic winds down for $n_e > 5 \times 10^{14}\,\text{cm}^{-3}$, the Mg II emission becomes unsuitable for measuring the rapid density rise to higher values (which generally happens at a given $z-$location when the magnetic field rises to a certain fraction of its peak magnitude). At these times, the density evolution was then studied utilizing B II and B III line-emission. The parameters obtained from the Mg II analysis were used to determine the initial conditions essential for the accurate simulation of the evolution of the boron line intensities.

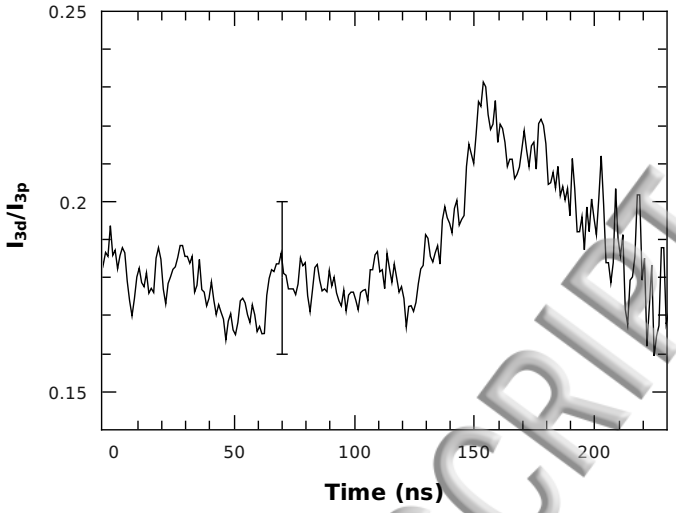

FIG. 2. Evolution of the line intensity ratio I_{3d}/I_{3p} measured at $z = 37\,\mathrm{mm}$. The term $Time = 0$ represents the beginning of the current-pulse.

A. Determination of the initial plasma properties

We tracked the intensities of the Mg II transitions $2p^6 3s - 2p^6 3p$ (I_{3p}) at 2795 Å and $2p^6 3p - 2p^6 3d$ (I_{3d}) at 2798 Å. The close wavelengths allow for their simultaneous recording using the same spectrograph. The propagating magnetic-field front arrives to the observed region (at $z = 37\,\mathrm{mm}$) $\sim 130\,\mathrm{ns}$ after the start of the current-pulse. Fig. 2 presents the evolution of the line intensity ratio I_{3d}/I_{3p}, starting from the the beginning of the current-pulse ($t = 0$), through the propagation of the magnetic front and its penetration into the dopant (positioned at $z = 37\,\mathrm{mm}$). The rise in the line-intensity ratio, observed for $t > 130\,\mathrm{ns}$, corresponds to an electron temperature and density rise that results from plasma pushing and heating by the magnetic field.

The line-intensity ratio I_{3d}/I_{3p} is most suitable for density diagnostics under hot ($T_e > 15$ eV) coronal conditions, since the ratio exhibits rather strong density dependence up to $n_e \sim 4 \times 10^{14}\,\mathrm{cm}^{-3}$, while it is nearly T_e-independent. However, here, the initial T_e is ≤ 10 eV[34], and thus I_{3d}/I_{3p} depends both on T_e and n_e. Thus, additional data are required for the diagnostics.

A second independent function of T_e and n_e is the Mg II ionization rate. If T_e and n_e are nearly constant and the change in the Mg II population is dominated by the Mg II ionization, then the normalized rate of the Mg II population change, $\frac{dn_{MgII}}{dt}/n_{MgII}$, is also constant and nearly independent of the ionization balance. Indeed, Mg I ionization into Mg II was verified to be negligible due to the low population of Mg I during the measurement, observed from the

intensity of the Mg I $3s-3p$ resonant transition at 2852 Å. The recombination from Mg III was calculated to be also negligible under the relevant plasma parameters. CR calculations further show that the Mg II resonant transition I_{3p} is proportional to the Mg II population. Therefore, the measured evolution of I_{3p} can be used to determine the Mg II ionization rate. We note that unlike the case of the line-intensity ratio, using the *derivative* of the intensity requires considering the possible effect of the dopant flow into the observed volume during the measurement. The dopant velocity in the positive x direction is $\sim 6\times10^5\,\mathrm{cm/s}$, thus the Mg ions travel less than 1 mm during the measurement time of 150 ns. Since the dopant column was found to be nearly uniform in a region of ±2 mm around the point of observation ($x = 10\,\mathrm{mm}$), the flow has no effect on the measured ionization rate. The normalized rate $\frac{\mathrm{d}\,I_{3p}}{\mathrm{d}\,t}/I_{3p}$ is presented in Fig. 3. As expected, until the arrival of the magnetic-field into the observed region ($t\sim130\,\mathrm{ns}$), the normalized Mg II ionization rate changes slowly compared to the rapid changes seen at later times.

The measured line-intensity ratio and the normalized intensity-change rate of I_{3p} are used to determine n_e and T_e at 65 ns (which is ~65 ns prior to the arrival of the magnetic-field front into the observed volume). The plasma parameters at this time are taken as the initial conditions for the B II-III simulations. CR calculations, including levels of Mg I (up to $n=4$), Mg II (up to $n=5$), and Mg III (ground level only), were employed for obtaining two sets of parameter pairs of n_e and T_e, each corresponding to the measured I_{3d}/I_{3p} and $\frac{\mathrm{d}\,I_{3p}}{\mathrm{d}\,t}/I_{3p}$. Each set of parameter-pairs defines a curve in the n_e-T_e space and the intersection of the two curves yields $T_e = 6.5\,\mathrm{eV}$ and $n_e = 2.1\times10^{14}\,\mathrm{cm^{-3}}$. In order to obtain the uncertainties in the measurement, we also calculated pairs of n_e and T_e that yield the lower and upper bounds of I_{3d}/I_{3p} and $\frac{\mathrm{d}\,I_{3p}}{\mathrm{d}\,t}/I_{3p}$ at $t=65\,\mathrm{ns}$. For the lower and upper bounds of the ratio I_{3d}/I_{3p} we take, respectively, 0.16 and 0.20. Here, the bounds are determined by the noise and possible systematic error in the relative calibration of the different PMT channels used for measuring the two wavelengths. For the lower and upper bounds of $\frac{\mathrm{d}\,I_{3p}}{\mathrm{d}\,t}/I_{3p}$ we take, respectively, -3×10^6 and $-2.5\times10^6\,\mathrm{s^{-1}}$. The n_e-T_e pairs corresponding to the lower and upper bounds on the measured I_{3d}/I_{3p} and the lower bound on $\frac{\mathrm{d}\,I_{3p}}{\mathrm{d}\,t}/I_{3p}$ are presented in Fig. 4 (the upper bound of $\frac{\mathrm{d}\,I_{3p}}{\mathrm{d}\,t}/I_{3p}$ is not useful for this analysis). A lower bound of 3 eV for T_e is obtained from the data. No practical upper bound on T_e exists. The absence of an upper-bound on T_e is due to the weak T_e-dependence of both the line ratio and the ionization rate at relatively high T_e. However, the data from the boron dopant, discussed in Section III B, provide tighter constraints on T_e: $4.5\,\mathrm{eV} < T_e < 8.5\,\mathrm{eV}$. These T_e bounds help to determine the bounds of n_e: $(1.3-3)\times10^{14}\,\mathrm{cm^{-3}}$. Thus, we conclude that ~65 ns prior to the arrival of the magnetic-field front $n_e = (2.1\pm0.8)\times10^{14}\,\mathrm{cm^{-3}}$ and $T_e = 6.5\pm2\,\mathrm{eV}$ (note that, as shown in Fig. 4, the errors in n_e and T_e are dependent on each other). These

This manuscript was accepted by Phys. Plasmas. Click here to see the version of record.

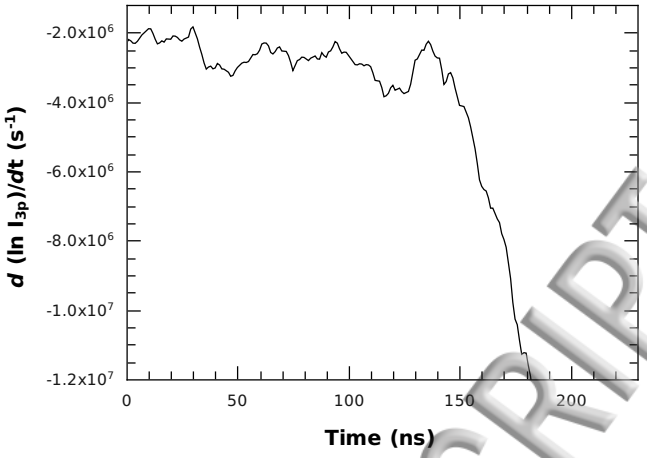

FIG. 3. Normalized rate of the change of the Mg II $2p^6 3s - 2p^6 3p$ line intensity ($\frac{\mathrm{d}(lnI_{3p})}{dt}$), representing the Mg II normalized ionization rate.

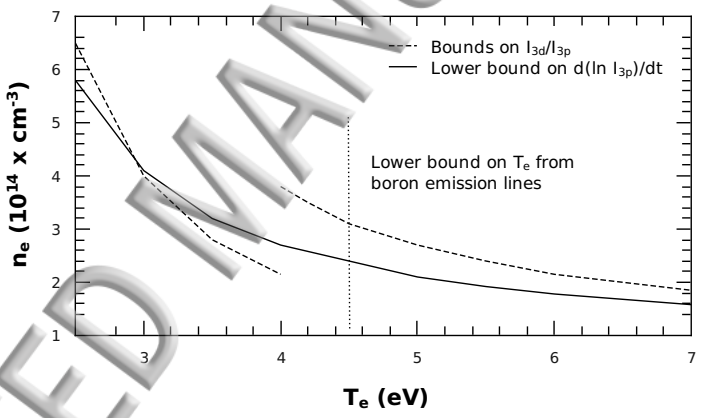

FIG. 4. Electron densities and temperatures that satisfy the lower and upper bounds of the intensity ratio I_{3d}/I_{3p} and the lower bound of the normalized Mg II ionization rate. The region above the solid curve and below the upper dashed curve corresponds to allowable n_e and T_e at $t = 65\,\mathrm{ns}$ (which is $\sim 65\,\mathrm{ns}$ prior to the magnetic-field arrival to the point of observation).

values are consistent with previous studies[34].

B. Density evolution during the plasma - magnetic field interaction

During the magnetic-field penetration the plasma parameters are extracted from the intensity evolution of the B II $2s2p - 2p^2$ (3451 Å) and B III $2s - 2p$ (2066 Å) transitions.

For utilizing these transitions, the B II/B III population ratio at $t = 65\,\mathrm{ns}$ must be estimated. This was achieved in two ways. In the first method, the measured intensity ratio $I_{3451\,\text{Å}}/I_{2066\,\text{Å}}$ was reproduced in CR modelling, constrained by the inferred n_e and T_e at $t = 65\,\mathrm{ns}$. In this manner a B III fraction between 10% to 40% was obtained. Here, the main source of error is the uncertainty in the wavelength dependent absolute calibration of the spectroscopic system. In the second method, we modelled the evolution of the B III fraction using the ionization rates under the slowly varying plasma conditions and assuming 100% B II at $t = -1\,\mu\mathrm{s}$ At this time, it was verified that the B I and B III populations were negligible by observing, respectively, the 2498 Å and 2066 Å lines. Under these conditions it was found that at $t = 65\,\mathrm{ns}$ the boron plume is mainly composed of B II and B III, where the B III fraction is between 10% to 35%. Both methods thus provided similar results. The uncertainties in the second method are due to uncertainties in the ambient plasma prefill conditions and in the initial population of the B II metastable level (that lies $\sim 4.6\,\mathrm{eV}$ above the ground state).

The intensities of the emission lines of both boron charge states were traced during the penetration of the magnetic field. The transition wavelengths are too remote from each other to be observed simultaneously by the same spectrograph, necessitating the correlation of their respective intensity evolutions recorded in different discharges. Achieving an accurate correlation here is of particular importance since, at this stage, when the plasma interacts with the field, the line intensities undergo rapid changes. Since the width of the magnetic-field front is $\sim 15\,\mathrm{mm}$ and the field propagation velocity[39] is $\sim 3 \times 10^7\,\mathrm{cm/s}$, the field front travels through the dopant column within $\sim 50\,\mathrm{ns}$. Hence, the accuracy of the temporal correlation must be at least 10 ns.

The approach adopted for accurately timing the evolutions of the B II and B III line intensities is based on the ions' Doppler-shifted line emissions and the assumption of the existence of an electrostatic potential hill that is the gradient of an electric field in the frame of the moving magnetic-field. This assumption is supported by recent measurements[39], showing that the electric- and magnetic-front profiles remain nearly constant during their propagation at the relevant time-scale of the measurement. The force exerted on an ion by such an electric field is proportional to the ion's charge, hence the ion's velocity change (in time) is proportional to its charge-to-mass ratio, Z/m. Assuming the ions are all in the same position, Z/m-scaled velocities of different ions should occur at the same time. Therefore, if for each ion the correlation between the evolutions of the ion velocity and its emission intensity is known, it is possible to time the emission intensity evolutions of different ions. Observations from the z-axis (along the direction of the magnetic-field propagation) provide this information.

Observed from the z-axis, the spectral-lines' Doppler-shifts are measured with the resolu-

high permitted by our discrete channel system; 0.12 Å per PMT-channel in this wavelength range. We identify the times t_{v_j} of the peak intensity of each of the time-dependent signals of the different Doppler-shifted emissions. At these times, the B II and B III at the plume center acquire the velocities v_j. In Fig. 5 we present the time-evolution of these intensity peaks. Each of the curves is obtained by averaging results over several discharges. The lines in the figure connect points corresponding to successive 0.12-Å wavelength shifts; the first point on the left in each curve is a shift of 0.06 Å. The curve for the B III emission is shifted in time such that a B III-Doppler shift of 0.36 Å coincides with the occurrence of a B II Doppler-shift of 0.30 Å, as required by the Z/m scaling, i.e., $\Delta\lambda \propto \lambda \times Z/m$, where λ and $\Delta\lambda$ are the wavelength and Doppler-shift. We stress that the Z/m scaling was performed for the ion acceleration that occurs rather early in the interaction. At later times of the plasma - magnetic-field interaction, the ionization of B II produces significant amount of relatively slow B III. The Figure also exhibits a non-monotonic B II velocity evolution at $t = 185$ ns, and two peaks in the time-dependent B III emission. These features are discussed in Sec. IV C.

Since we find that at each instant most of emission of each ion comes from a specific velocity, the two curves in Fig. 5 are, in fact, the intensity evolution of the B II and B III line emissions, sampled at specific times corresponding to specific velocities. Moreover, since the y-axis observation is also aimed at the dopant plume center, both the y- and the z-axis observations collect data from the same volume. Thus, we can take the time difference between the B II and B III intensity peaks observed in the z direction to be equal to the time difference between the peaks of the B II and B III emission intensities observed in the y direction. The y-axis observations are more useful for modeling due to the ability for a continuous comparison beyond the discrete times t_{v_j}. As seen in Fig. 5, we obtain a time difference of $\delta t = 9 \pm 5$ ns between the peaks of the B II and B III emission intensities. The errors in the timing are mainly due to the limited dispersion of the spectroscopic system and the difficulty in determining the time of the peak of the signal from the first Doppler-shifted channel (the signal peak of this channel is smeared out since it has an appreciable intensity already before the current-pulse arrival due to the initial spectral line-width).

The correlated time-dependent intensities of the two boron lines, observed in the y-direction, were fitted simultaneously with the same electron temperature and density evolution. We note that in our models we assume that the electron population has a Maxwellian distribution. The possible presence of a high-energy electron beam[40] should not significantly change the conclusions on the density evolution since its effect on these transitions is rather similar to that of a high temperature. We emphasize that in our approach the analysis of the B II and B III emission intensities is solely based on the time-evolution of the emission,

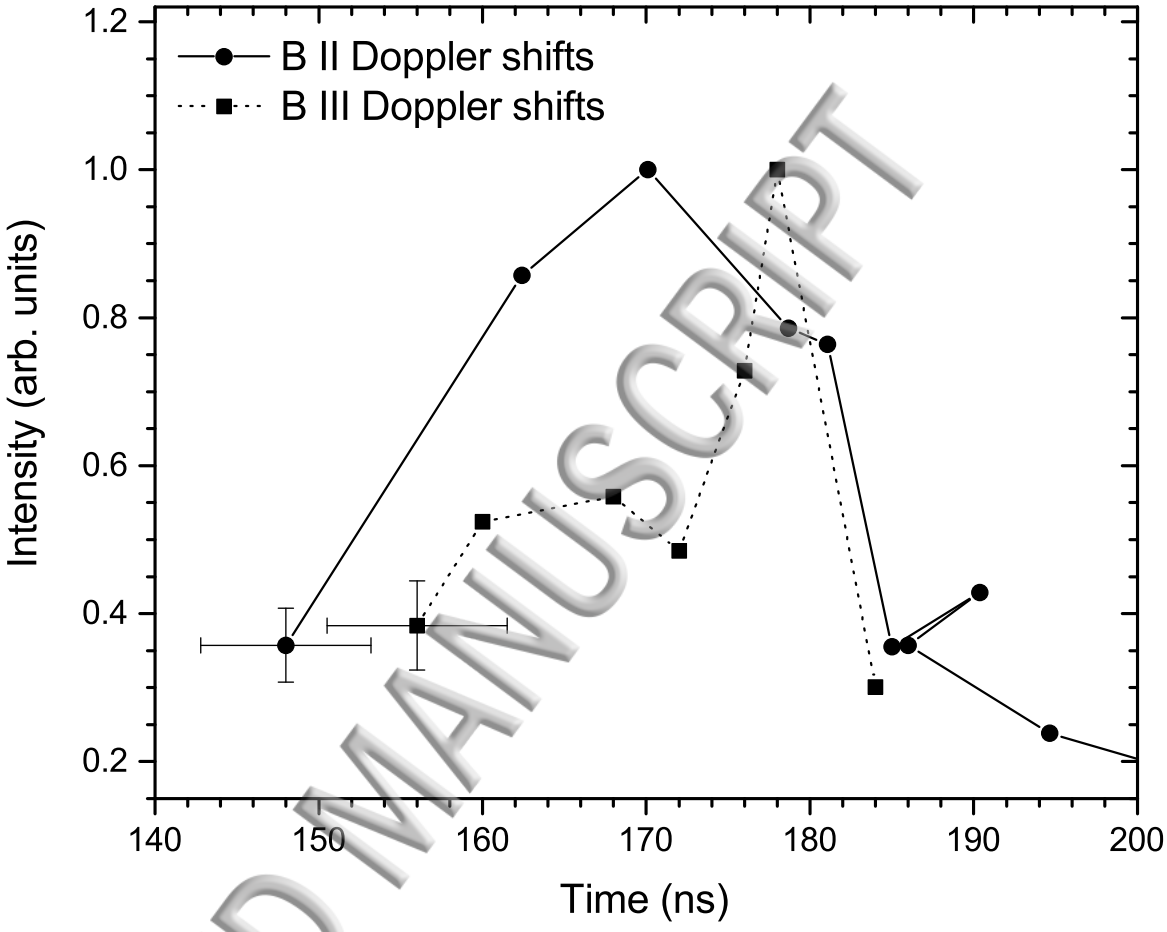

FIG. 5. Evolution of the B II and B III line intensities during the penetration of the magnetic field, observed in the z-direction (along the field propagation direction). The times of the points are the times at which the intensity of each Doppler-shifted signal (in 0.12-Å steps) peaks. The curves connect the points of consecutive wavelength-shifts. The first point on the left in each curve is a shift of 0.06 Å from the zero velocity wavelength. The B III curve is shifted in time so that the wavelength shifts of 0.3 Å for B II and 0.36 Å for B III occur at the same time.

and not on the absolute intensities that may be subjected to an appreciable shot-to-shot variations due to differences in the amount of dopant.

Several initial electron temperature-density pairs were tested, all consistent with the constraints set by the Mg II-line-emission measurements. In Fig. 6 we present the experimental results together with the simulations. For the low limit of the initial electron temperature

of 4.5 eV, no reasonable fit for the boron emission lines could be obtained. The ionization rate of B II for such low temperature was too small to explain the observed rise of the B III emission intensity. Assuming rapid rise of the temperature, to satisfy the B III data, leads to an overestimate of the B II emission, even when starting with the lowest reasonable fraction of B III ions (B III = 10%). This is demonstrated in Fig. 6(a), where the best fit obtained for this low initial T_e yielded poor agreement with the experimental data: simulated emission that is too low for B III and too high for B II. For the most likely values of initial parameters, $n_e \sim 2.1 \times 10^{14}\,\mathrm{cm}^{-3}$, $T_e \sim 6.5\,\mathrm{eV}$, and an initial B III fraction of 20%, a good fit for both B II and B III can be obtained, as shown in Fig. 6(b). The figure also presents the measured intensity evolution of an O III transition (3455 Å), with an upper level at 49 eV, observed simultaneously with the B II line. The intensity evolution of this O III transition indicates that the heating of the electrons to energies of tens of eVs occurs only after $t \sim 170\,\mathrm{ns}$. Models with initial high T_e ($> 8.5\,\mathrm{eV}$) are ruled out since prior to the arrival of the magnetic field such models give a rise in time of the B III intensity (due to B II ionization) that is much more rapid than observed (for any reasonable initial density and B III fraction).

The evolutions of n_e and T_e used for obtaining a good fit are shown in Fig. 7. In this model, the electron density rises to a peak of $\sim 10^{15}\,\mathrm{cm}^{-3}$, which is about 5 times higher than the electron density prior to the magnetic field arrival. The electron temperature in the model rises to 50 eV at $t = 165\,\mathrm{ns}$. Above 50 eV, the two boron line-intensities become nearly insensitive to T_e, and our choice to adopt a further rise of T_e is based on a previous study[40] that utilizes the emission from a high-energy transition of B IV, indicating a rise of the electron energy to 250 eV at $t \sim 175\,\mathrm{ns}$. Information on the T_e evolution at later times is absent, but the fact that the O III emission does not drop implies that T_e drops to below $\sim 70\,\mathrm{eV}$ (otherwise the O III would undergo rapid ionization).

The apparent local peak observed in the experimental line-intensity evolution of both B II and B III (see Fig. 6, $t \sim 155\,\mathrm{ns}$) is attributed to a density change. However, it may also be fitted with a T_e change. We claim it is a density effect based on the inferred plasma dynamics, as discussed in Sec. IV C.

So far, we have shown that the evolution of the plasma parameters presented in Fig. 7 provides a plausible explanation for the observed line intensities. However, in principle, this explanation might not be unique. In particular, one may argue that the sharp intensity rise of the boron line emissions could be the result of a rise in T_e, and that a good fit to the observation may also be obtained without a significant rise in n_e. In order to rule out such a scenario, we have carried out simulations in which the T_e evolution was optimized to yield the maximum intensity from the boron lines at the correct time. These simulations have

This manuscript was accepted by Phys. Plasmas. Click here to see the version of record.

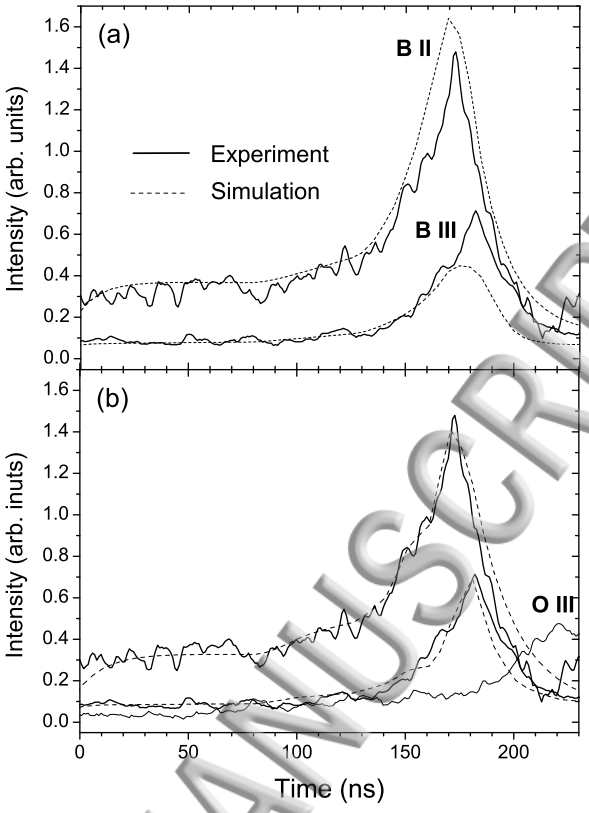

FIG. 6. Observed and simulated evolutions of the B II (3451 Å) and B III (2066 Å) intensities. (a) Initial parameters assumed are $T_e = 4.5\,\mathrm{eV}$, $n_e = 3.2 \times 10^{14}\,\mathrm{cm}^{-3}$, and 10% B III. (b) The optimal fit found to the observation. Initial parameters assumed are $T_e = 6.5\,\mathrm{eV}$, $n_e = 2.1 \times 10^{14}\,\mathrm{cm}^{-3}$, and 20% B III. Also presented is the intensity of O III transition (with an upper level of unit[49]eV), observed simultaneously with the B II transition.

shown that even such an optimized T_e cannot account for the observed rise in the boron intensities unless it is accompanied by a significant density rise to $\sim 10^{15}\,\mathrm{cm}^{-3}$.

We have found that the main factor affecting the estimate of the electron-density evolution is the initial B III fraction, which is in the range between 10% to 35%. This range of assumed B III fractions provides bounds on the peak electron density, based on the following considerations: The experimental emission intensity of the B II line rises by a factor of 5 between $t = 50\,\mathrm{ns}$ to $t = 170\,\mathrm{ns}$. This rise is partly due to the change in T_e. Assuming constant n_e and a T_e-rise to 15 eV, which maximizes the intensity rise due to a T_e-rise, gives a B II intensity-rise of a factor of only 2.2. Hence, the rise of the B II emission intensity due to the n_e-rise is at least by a factor 2.3. We now must also consider the effect of ionization of B II, which lowers the B II emission as T_e rises to 15 eV. To obtain the effect of the B II

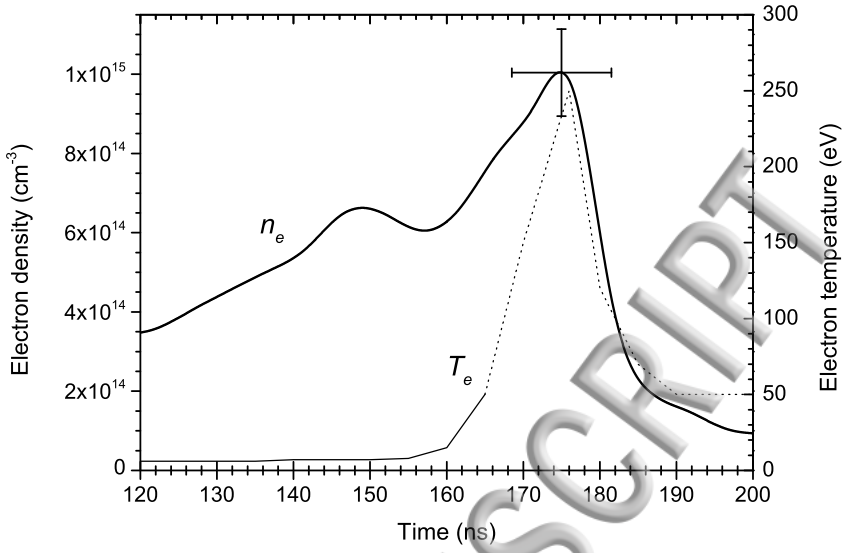

FIG. 7. The inferred evolution of n_e and T_e. For $t \geq 165$ ns, T_e is only an estimate (marked by the dotted curve), but has no significant effect on the present B II - III modelling. The error bars reflect only the errors due to the uncertainties in the initial n_e and T_e, and not the uncertainty in the B II/B III ratio.

ionization during these 120 ns, we use the B III emission intensity that rises by a factor 6 during this time. In order to obtain a lower bound for the rise of n_e, we assume a maximal effect of B II ionization on B III, namely, we consider a minimal initial B III fraction of 15%. Under these assumptions, the observed B III emission-intensity rise requires n_e-rise of nearly a factor of 3, yielding a robust lower bound of $6.3 \times 10^{14}\,\mathrm{cm}^{-3}$ for the peak n_e. Using a detailed modelling assuming an initial fraction of 15% B III, the best fit to the experimental data is obtained when n_e rises to $8 \times 10^{14}\,\mathrm{cm}^{-3}$. Similarly, an upper bound for n_e is obtained by assuming an initial T_e of 8.5 eV and B III fraction of 35%, yielding a peak electron density of $1.5 \times 10^{15}\,\mathrm{cm}^{-3}$.

IV. DISCUSSION

One of the difficulties that arose from previous measurements is the quantitative explanation of the measured density profile[30]. It was shown, under similar conditions, that ionization processes (due to the electron heating resulting from the magnetic energy dissipation) and the continuous plasma flow from the flashboard-plasma source cannot account for more than $\sim 30\%$-rise in n_e during the magnetic field penetration. The significant addi-

inital density-rise observed was attributed to the proton reflection; a process later verified using charge exchange measurements[31]. The subsequent density drop could not have been explained by the proton reflection only. The present, high-resolution measurements, that show a much larger density-rise and a faster subsequent density-drop, thus call for a revisit of the underlying processes, which can now be performed using the correlation between the electron density and the ion velocity.

A. Dynamics of different ion-species

We now explore the connection between the density observation and the ion dynamics. Our analysis here is based on the assumption of the existence of an electric field that in the frame of the moving magnetic field is the gradient of an electrostatic potential hill. Under this condition we can utilize the measured evolution of the B II ion-dopant velocity to infer the dynamics of all other ions, and in particular to determine the expected reflection points of the various ion-species. From energy conservation we write for B II:

$$eZ_{BII}\phi = \frac{1}{2}m_{BII}\left(v_b^2 - \tilde{v}_{BII}^2\right), \tag{1}$$

where Z_{BII} and m_{BII} are, respectively, the B II ionization degree and mass. ϕ is the electrostatic potential ($\phi = 0$ in the foot of the potential hill), e is the elementary charge, v_b is the magnetic-field propagation velocity, and $\tilde{v}_{BII}$ is the B II velocity in the moving field frame. Since all ions move under the same potential, we can write for an ion i:

$$\frac{m_{BII}}{Z_{BII}}\left(v_b^2 - \tilde{v}_{BII}^2\right) = \frac{m_i}{Z_i}\left(v_b^2 - \tilde{v}_i^2\right) \tag{2}$$

At the reflection point of ion i, its velocity in the moving magnetic-field frame is $\tilde{v}_i = 0$. Thus, taking $\tilde{v}_i = 0$ in Eq. 2, we obtain $v_{BII}^{ref(i)}$, the B II velocity (in the laboratory frame) at the reflection point of an ion i:

$$v_{BII}^{ref(i)} = v_b\left(1 - \sqrt{1 - \frac{Z_{BII}}{m_{BII}}\frac{m_i}{Z_i}}\right). \tag{3}$$

We now use the measured B II velocity evolution and its correlation with the density evolution to find the predicted reflection times of the various ion-species on the density evolution curve. For a magnetic-field propagation velocity[39] $v_b = 3\times10^7$ cm/s, we obtain from Eq. 3 that the protons, the C V, and the C IV are reflected, respectively, when the B II acquires velocities of 1.4×10^6, 4.5×10^6, and 6.2×10^6 cm/s. On the other hand, the C III and C II reflection points correspond, respectively, to $v_{BII} = 10^7$ cm/s and $v_{BII} = 2.2\times10^7$ cm/s, that are *higher* than the maximum measured B II velocity of 9.5×10^6 cm/s, which

means that the C III and C II plasmas are penetrated by the magnetic field. In Fig. 8 we present the measured evolutions of the electron density and the B II velocity, together with the expected reflection times of the protons and C IV-V.

Since an ion reflection is associated with a density peak, the expected reflection times seen in Fig. 8 suggest that the main density peak ($t = 175$ ns) is attributed to the reflection of the carbon ions, whereas the earlier, local density peak ($t = 146$ ns) corresponds to the proton reflection. The reflection times marked in Fig. 8 appear ~ 10 ns after the observed density peaks, but it is within the uncertainty of the experimental results (mainly due to the systematic errors in the determination of the times of the B II velocity values and an uncertainty in v_b). In fact, the reflection process of each ion species occurs over a finite time due to the ion initial-velocity distribution, prior to the application of the magnetic field. Ions with an initial velocity in the direction of the field-propagation direction are reflected by a lower electric potential than those with an initial velocity directed opposite the field-propagation direction. This effect is considered in Section IV B.

B. Simulated electron density profile

The inferred ion dynamics, together with the known plasma composition and initial ion velocity distribution[34], allow for deriving the electron density evolution and examine whether the potential hill assumption is consistent with the measured density. If the ionization rate of the plasma constituents is negligible, then the density evolution of each ion species in the plasma is determined by the change in the velocity distribution of that ion species. The equations that describe the change of the density as a function of the ion position in the potential hill are given in the Appendix. The plasma composition is taken from a previous study[34], but scaled here by a factor of 0.7 to account for minor modifications in the experimental set-up. Thus, the initial ion density are: $n_p = 3.5 \times 10^{13}\,\mathrm{cm}^{-3}$, $n_{CII} = 9.1\times10^{12}\,\mathrm{cm}^{-3}$, $n_{CIII} = 1.5\times10^{13}\,\mathrm{cm}^{-3}$, $n_{CIV} = 4.9\times10^{13}\,\mathrm{cm}^{-3}$, and $n_{CV} = 1.4\times10^{13}\,\mathrm{cm}^{-3}$. The initial ion-velocity spread along the z-axis, Δv_z, is approximated by $v_2 \sin(\pi/8)$, where v_2 is the injection velocity (along the x-axis). v_2 is in the range $\sim 10^6 - 10^7$ cm/sec, depending on the ion species[34].

Fig. 9 presents the simulated ion densities, together with the resulting electron density (convolved with the finite temporal response of the spectroscopic system), compared to the measured density. It is seen from the Figure that besides differences of 7 - 10 ns in the times of the peaks, which are within the measurement uncertainty, the simulated electron density recovers the evolution obtained from the independent measurement. This result demonstrates that the ion dynamics can explain the observed density evolution, and thus

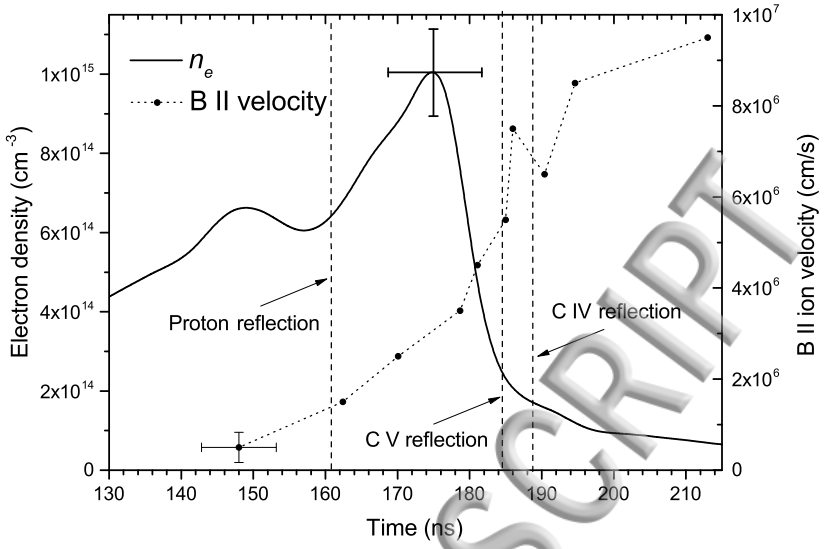

FIG. 8. The electron density and B II velocity evolutions and the expected reflection times for protons, C V and C IV, extrapolated from the B II ion velocities assuming a potential hill in the moving frame of the magnetic field. The representative time-error of the velocities represents the systematic error due to the uncertainty in the determination of the velocity evolution relative to the density evolution. The uncertainties of the relative times of the velocities are much smaller, less than 3 ns.

strongly supports the existence of an electric potential hill.

C. Observations along different directions

While the B III emission, observed along the z-axis (see Fig. 5), exhibits a clear double-peak feature that corresponds to the proton and C IV-V reflections, observations along the y-axis mainly exhibit a single prominent peak emission and a "shoulder" (see Fig. 6, $t \sim 150$ ns). We attribute this difference to the fact that the y-axis observations use a *single* PMT to record the evolution of the emission intensity, whereas in the z-axis observations, each of the points of the intensity-evolution curve is the peak of the signal measured by a *different* PMT, corresponding to the different Doppler-shifted wavelengths. This sampling of signals using different PMTs enables us to avoid some of the signal smearing due to the PMT decay time (5 ns). Note that the B II emission recorded along the z-axis does not exhibit the earlier peak (attributed to the proton reflection) since the proton reflection occurs before the B II is accelerated to a velocity that can be unambiguously measured within the present

This manuscript was accepted by Phys. Plasmas. Click here to see the version of record.

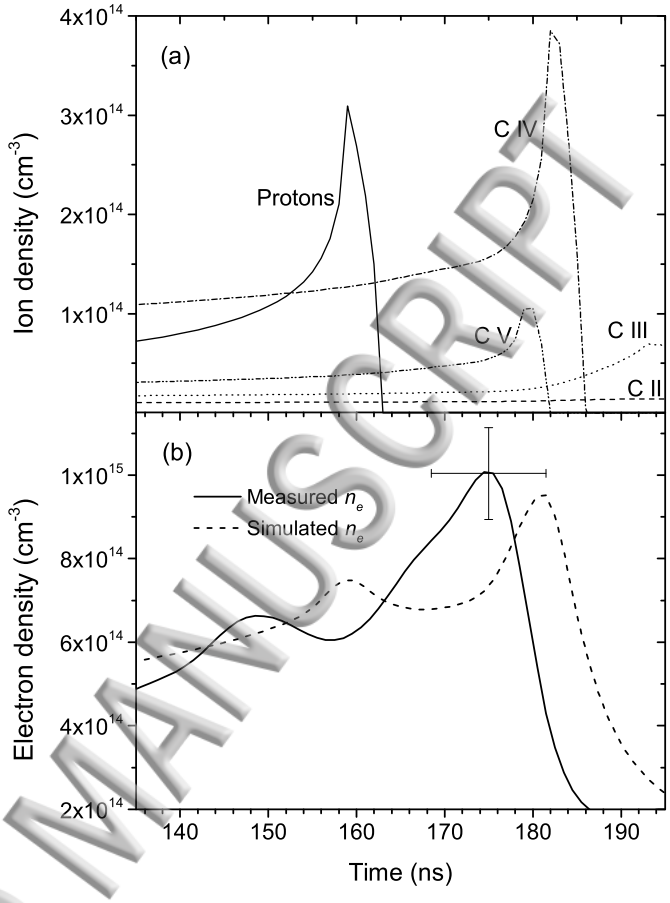

FIG. 9. (a) The simulated density evolution of the various ion-species based on the measured B II velocity and the assumption of a potential hill (see Appendix) and (b) the resulting electron density evolution (convolved with the finite temporal response of the spectroscopic system), compared with the measured electron density.

spectral resolution. The proton reflection occurs when the B II Doppler shift is ~ 0.15 Å, which is comparable to the 0.12-Å resolution, whereas the B III Doppler shift at this time is ~ 0.20 Å.

Interestingly, the B II velocity evolution indicates a non-monotonic behaviour (Fig. 5, $t = 185$ ns), in which a higher velocity appears before a lower one. The apparent absence of a low-velocity value is likely a result of a combination of the rapid acceleration and the limited temporal-response of the spectroscopic system. However, the appearance of a lower velocity

at a later time, a phenomenon observed in a large percent of the discharges, may arise from a 2D or 3D effect and could indicate a fluctuation in the magnetic-field (as suggested, for example, in a recent simulation[28]).

V. CONCLUSIONS

This study presents high-spatial-resolution spectroscopic measurements of the electron density evolution during the propagation of a magnetic field into a low-resistivity, *multi-ion species* plasma. The electron density evolution is inferred from the intensity evolution of emission lines of dopant ions injected into the ambient plasma. The spatial resolution achieved in these measurements is below 1 mm in the x- and z-axes (the y-axis is the symmetry axis and thus an axis of nearly constant properties). Upon the arrival of the magnetic field to the observed volume, the present measurements reveal a density-rise that is much more pronounced, and a subsequent density-drop that is much faster than those observed in previous lower-resolution measurements[30].

The Dopant ion-velocity data are analysed and used to predict the plasma dynamics, assuming the existence of an electric potential hill in the propagating magnetic-field reference frame. This analysis also yields a prediction of the electron density evolution, which is found to be consistent with the independent density measurements. The data used are the time-dependent axial velocity of B II (the dopant ion). The scenario we envision is the slowing down of the various ion-species as they climb the potential hill (in the magnetic-field frame). The protons, C V, and C IV reach a complete stop at different potential heights, according to their charge-to-mass ratios. In the laboratory reference frame, these are the turning points for the ion reflections. Detailed simulations of the ion densities and the resulting electron density show that the ion dynamics explains the observed density; the main density peak is a result of the C IV-V reflection, whereas an earlier, local peak, results from the proton reflection. The potential hill is not high enough to stop the C III and other ions with similar or smaller charge-to-mass ratios. In the laboratory frame, the plasma of these ion-species is penetrated by the magnetic field.

We stress that unlike the reflection of the protons that was directly observed by means of charge-exchange techniques[31], the inferred reflection of C IV-V depends on the validity of the electric-potential hill model. We note that other possible phenomena, such as instabilities or other 3D effects, as well as energetic electrons ejected from the electrodes, may also play a role in the interaction and their investigation may require better resolutions.

This manuscript was accepted by Phys. Plasmas. Click here to see the version of record.

ACKNOWLEDGMENTS

The work is supported in part by the Minerva Foundation with funding from the Federal German Ministry for Education and Research, by the U.S.-Israel Bi-national Science Foundation (BSF), and by the Naval Research Laboratory (USA).

Appendix A: Derivation of the ion densities

We use the initial ion-velocity distribution function for calculating the plasma density during the penetration of the magnetic field. The ions are injected in the x direction. The ith ion-species velocity distribution function in the moving frame before the arrival of the potential hill is:

$$\widetilde{f}_i\left(v_x,v_y,v_z\right)=g\left(v_x\right)h\left(v_y\right)f_i\left(v_z\right). \tag{A1}$$

The initial velocity distribution functions are assumed to be spatially uniform. Since the plasma ions are not magnetized and assuming the electric field is directed along the z-axis, g and h do not vary along the ion trajectory in z. We choose g and h to be $\int_{-\infty}^{\infty}dv_x g\left(v_x\right)=\int_{-\infty}^{\infty}dv_y h\left(v_y\right)=1$ so that the ion-density evolution follows the evolution of f_i. Since the potential hill moves in the z direction with the velocity v_b (>0) it is stationary in the moving frame, where all ions move towards the potential hill with an average velocity $-v_b$, so that

$$f_i\left(v_z\right)=\frac{n_{i0}}{2\Delta v_z}\left[H\left(\frac{v_z}{v_b}+1+\frac{\Delta v_z}{v_b}\right)-H\left(\frac{v_z}{v_b}+1-\frac{\Delta v_z}{v_b}\right)\right], \tag{A2}$$

where H is the Heaviside function and n_{i0} is the density of the ith ion-species before the arrival of the potential hill. The divergence angle of the ions injected along x results in a velocity spread Δv_z, approximated by $v_2\sin\left(\pi/8\right)$, where v_2 is the average plasma injection velocity from the plasma source. The distribution function is a function of the energy that is a constant of the ion motion, and thus satisfies $f_i\left(v_z,\phi\right)=f_i\left(-\sqrt{v_z^2+2Z_i e\phi/mA_i},\phi=0\right)$, where Z_i and A_i are the charge and the atomic number of the ith ion-species, and m is the proton mass. In the presence of the potential hill, the ith ion-species density is, therefore

$$\begin{aligned}n_i\left(\phi\right)=\frac{n_{i0}v_b}{2\Delta v_z}\int_{-\infty}^{0}d\xi\Bigg[&H\left(-\sqrt{\xi^2+\frac{2Z_i e\phi}{A_i m v_b^2}}+1+\frac{\Delta v_z}{v_b}\right)-\\&H\left(-\sqrt{\xi^2+\frac{2Z_i e\phi}{A_i m v_b^2}}+1-\frac{\Delta v_z}{v_b}\right)\Bigg],\end{aligned} \tag{A3}$$

This manuscript was accepted by Phys. Plasmas. Click here to see the version of record.

where we define $\xi = v_z/v_b$. The last integral is transformed into

$$n_i(\phi) = -\frac{n_{i0}v_b}{2\Delta v_z}\int_{-\infty}^{-\sqrt{2Z_ie\phi/A_imv_b^2}} ds \frac{s}{\sqrt{s^2-(2Z_ie\phi/A_imv_b^2)}} \times \left[H\left(s+1+\frac{\Delta v_z}{v_b}\right) - H\left(s+1-\frac{\Delta v_z}{v_b}\right)\right]. \tag{A4}$$

We denote the height of the potential hill by ϕ_0. There are three possibilities for each ion species: (a) full penetration of the magnetic field, (b) full reflection of the ions, and (c) penetration of the magnetic field into part of the ions and reflection of the other part. In the first case:

$$-\sqrt{\frac{2Z_ie\phi_0}{A_imv_b^2}} + 1 - \frac{\Delta v_z}{v_b} > 0, \tag{A5}$$

there is full penetration, and all the ions of the ith species climb the potential hill. Performing the integral, we obtain the densities of these ions

$$\begin{aligned} n_i(\phi) &= -\frac{n_{i0}v_b}{2\Delta v_z}\int_{-1-\Delta v_z/v_b}^{-1+\Delta v_z/v_b} ds \frac{s}{\sqrt{s^2-(2Z_ie\phi/A_imv_b^2)}} \\ &= \frac{n_{i0}v_b}{2\Delta v_z}\left[\sqrt{\left(1+\frac{\Delta v_z}{v_b}\right)^2 - \frac{2Z_ie\phi}{A_imv_b^2}} - \sqrt{\left(1-\frac{\Delta v_z}{v_b}\right)^2 - \frac{2Z_ie\phi}{A_imv_b^2}}\right]. \end{aligned} \tag{A6}$$

We note that if

$$\frac{\Delta v_z}{v_b} \ll 1 - \frac{2Z_ie\phi}{A_imv_b^2}, \tag{A7}$$

the density of the penetrated-plasma ions is approximately

$$\begin{aligned} n_i(\phi) &= \frac{n_{i0}v_b}{2\Delta v_z}\left[\sqrt{1-\frac{2Z_ie\phi}{A_imv_b^2}+\frac{2\Delta v_z}{v_b}} - \sqrt{1-\frac{2Z_ie\phi}{A_imv_b^2}-\frac{2\Delta v_z}{v_b}}\right] \\ &\approx \frac{n_{i0}v_b}{2\Delta v_z}\sqrt{(1-(2Z_ie\phi/A_imv_b^2))}\left[\frac{2\Delta v_z}{v_b(1-(2Z_ie\phi/A_imv_b^2))}\right] \\ &= \frac{n_{i0}}{\sqrt{1-(2Z_ie\phi/A_imv_b^2)}}, \end{aligned} \tag{A8}$$

which is that of a cold ion-beam.

The second case is that of a full reflection. This happens if

$$-\sqrt{\frac{2Z_ie\phi_0}{A_imv_b^2}} + 1 + \frac{\Delta v_z}{v_b} < 0. \tag{A9}$$

The density of the ions is composed of both ions climbing the hill and of those reflected. In this case of full reflection, there are three different regimes. While the potential satisfies

$$-\sqrt{\frac{2Z_i e\phi}{A_i m v_b^2}}+1-\frac{\Delta v_z}{v_b}>0, \tag{A10}$$

all ions of the ith ion-species climb beyond this potential. The ion density at these values of the potential is given by (twice that of Eq. A6 to account for both the climbing and reflected ions):

$$n_i\left(\phi\right)=\frac{n_{i0}v_b}{\Delta v_z}\left[\sqrt{\left(1+\frac{\Delta v_z}{v_b}\right)^2-\frac{2Z_i e\phi}{A_i m v_b^2}}-\sqrt{\left(1-\frac{\Delta v_z}{v_b}\right)^2-\frac{2Z_i e\phi}{A_i m v_b^2}}\right]. \tag{A11}$$

Then, while the potential satisfies

$$1+\frac{\Delta v_z}{v_b}>\sqrt{\frac{2Z_i e\phi}{A_i m v_b^2}}>1-\frac{\Delta v_z}{v_b}, \tag{A12}$$

part of the ions are reflected before reaching these potential values, and only the more energetic ions contribute to the density in this regime:

$$\begin{aligned} n_i\left(\phi\right)&=-\frac{n_{i0}v_b}{\Delta v_z}\int_{-1-\Delta v_z/v_b}^{-\sqrt{2Z_i e\phi/A_i m v_b^2}}ds\frac{s}{\sqrt{s^2-\left(2Z_i e\phi/A_i m v_b^2\right)}} \\ &=\frac{n_{i0}v_b}{\Delta v_z}\left[\sqrt{\left(1+\frac{\Delta v_z}{v_b}\right)^2-\left(\frac{2Z_i e\phi}{A_i m v_b^2}\right)}\right]. \end{aligned} \tag{A13}$$

For higher values of the potential,

$$\sqrt{\frac{2Z_i e\phi}{A_i m v_b^2}}>1+\frac{\Delta v_z}{v_b}\Longrightarrow n_i=0. \tag{A14}$$

No ions reach such high potential.

The third case is when the peak of the potential, ϕ_0, satisfies

$$1+\frac{\Delta v_z}{v_b}>\sqrt{\frac{2Z_i e\phi_0}{A_i m v_b^2}}>1-\frac{\Delta v_z}{v_b}. \tag{A15}$$

In this case, part of the ith ion-species plasma is penetrated and the rest is reflected. In our experiment, this situation does not seem to apply to any of the ion species.

[1]M. Rosenbluth, in *Progress in Nuclear Energy, Series XI*, Vol. 2, edited by J. T. T. C. L. Longmire and W. B. Thompson (Pergamon, Londonk, 1963).

[2]N. A. Krall and A. W. Trivelpiece, *Principle of Plasma Physics* (McGraw Hill, New York, 1973) p. 124.

[3]J. Wesson and D. J. Campbell, *Tokamak* (Oxforde University Press, 1997).

[4]R. J. Commisso and H. R. Griem, Physics of Fluids (1958-1988) **20**, 44 (1977).

[5]P. Bogen and E. Hint, in *Gaseous Electronics*, Vol. 1, edited by M. N. Hirsh and H. J. Oskam (Academic Press, New York, 1978).

[6]T. A. Mehlhorn, IEEE Transactions on Plasma Science **25**, 1336 (1997).

[7]IEEE Trans. Plasma Sci. **PS-15** (1987), and references therein.

[8]W. Peter, A. Ron, and N. Rostoker, Physics of Fluids (1958-1988) **26**, 2276 (1983).

[9]S. B. Mende, G. R. Swenson, S. P. Geller, J. H. Doolittle, G. Haerendel, A. Valenzuela, and O. H. Bauer, Journal of Geophysical Research: Space Physics **94**, 17063 (1989).

[10]M. J. Aschwanden, A. I. Poland, and D. M. Rabin, Annual Review of Astronomy and Astrophysics **39**, 175 (2001).

[11]K. J. H. Phillips, Plasma Physics and Controlled Fusion **42**, 113 (2000).

[12]C. Litwin, R. Rosner, and D. Q. Lamb, Monthly Notices of the Royal Astronomical Society **310**, 324 (1999).

[13]A. S. Kingsep, Y. V. Mohkov, and K. V. Chukbar, Sov. J. Plasma Phys. **10**, 495 (1984).

[14]A. S. Kingsep, K. V. Chukbar, and V. V. Yankov, *Reviews on plasma Physics*, edited by B. Kadomtsev, Vol. 16 (Consultants Review, New York, 1990) p. 243.

[15]A. Fruchtman, Physics of Fluids B: Plasma Physics (1989-1993) **3**, 1908 (1991).

[16]K. Gomberoff and A. Fruchtman, Physics of Fluids B: Plasma Physics (1989-1993) **5**, 2841 (1993).

[17]A. V. Gordeev, A. S. Kingsep, and L. I. Rudakov, Physics Reports **243**, 215 (1994).

[18]J. J. Moschella, C. C. Klepper, C. Vidoli, E. J. Yadlowsky, B. V. Weber, R. J. Commisso, D. C. Black, B. Moosman, S. J. Stephanakis, D. D. Hinshelwood, and Y. Maron, Phys. Plasmas **12**, 023102 (2005).

[19]E. M. Waisman, P. G. Steen, D. E. Parks, and A. Wilson, Applied Physics Letters **46**, 1045 (1985).

[20]J. M. Grossmann, P. F. Ottinger, J. M. Neri, and A. T. Drobot, Physics of Fluids **29**, 2724 (1986).

[21]J. M. Grossmann, P. F. Ottinger, and R. J. Mason, Journal of Applied Physics **66**, 2307 (1989).

[22]J. D. Huba, J. M. Grossmann, and P. F. Ottinger, Physics of Plasmas **1**, 3444 (1994).

[23]A. Fruchtman, J. M. Grossmann, S. B. Swanekamp, and P. F. Ottinger, IEEE Transactions on Plasma Science **27**, 1464 (1999).

[24]N. Jain, A. Das, S. Sengupta, and P. Kaw, Physics of Plasmas **19**, 092305 (2012), http://dx.doi.org/10.1063/1.4751872.

[25]S. B. Swanekamp, J. M. Grossmann, A. Fruchtman, B. V. Oliver, and P. F. Ottinger, Physics of Plasmas **3**, 3556 (1996).

[26]J. R. Angus, A. S. Richardson, P. F. Ottinger, S. B. Swanekamp, and J. W. Schumer, Physics of Plasmas **21**, 112306 (2014), http://dx.doi.org/10.1063/1.4902101.

[27]A. Richardson, J. Angus, S. Swanekamp, P. Ottinger, and J. Schumer, Plasma Science, IEEE Transactions on **42**, 2552 (2014).

[28]A. S. Richardson, J. R. Angus, S. B. Swanekamp, I. M. Rittersdorf, P. F. Ottinger, and J. W. Schumer, Physics of Plasmas **23**, 052110 (2016), http://dx.doi.org/10.1063/1.4948715.

[29]A. Weingarten, R. Arad, Y. Maron, and A. Fruchtman, Physical Review Letters **87**, 115004 (2001).

[30]R. Arad, K. Tsigutkin, Y. Maron, A. Fruchtman, and J. D. Huba, Physics of Plasmas (1994-present) **10**, 112 (2003).

[31]R. Arad, K. Tsigutkin, Y. Maron, and A. Fruchtman, Physics of Plasmas (1994-present) **11**, 4515 (2004).

[32]D. Hinshelwood, B. Weber, J. M. Grossmann, and R. J. Commisso, Phys. Rev. Lett. **68**, 3567 (1992).

[33]A. Chuvatin and B. Etlicher, Phys. Rev. Lett. **74**, 2965 (1995).

[34]R. Arad, K. Tsigutkin, Y. V. Ralchenko, and Y. Maron, Physics of Plasmas (1994-present) **7**, 3797 (2000).

[35]J. F. Friichtenicht, Review of Scientific Instruments **45**, 51 (1974).

[36]S. Mattoo, L. Wirtz, A. Pospieszczyk, and B. Schweer, Nuclear Instruments and Methods in Physics Research Section B: Beam Interactions with Materials and Atoms **124**, 579 (1997).

[37]V. Schultze and M. Wagner, Applied Physics A **53**, 241 (1991).

[38]Y. V. Ralchenko and Y. Maron, Journal of Quantitative Spectroscopy and Radiative Transfer **71**, 609 (2001), radiative Properties of Hot Dense Matter.

[39]B. Rubinstein, R. Doron, Y. Maron, A. Fruchtman, and T. A. Mehlhorn, Physics of Plasmas **23**, 040703 (2016), http://dx.doi.org/10.1063/1.4947220.

[40]R. Doron, R. Arad, V. Bernshtam, Y. Maron, and Y. Ralchenko, Physical Review E **78**, 036410 (2008).

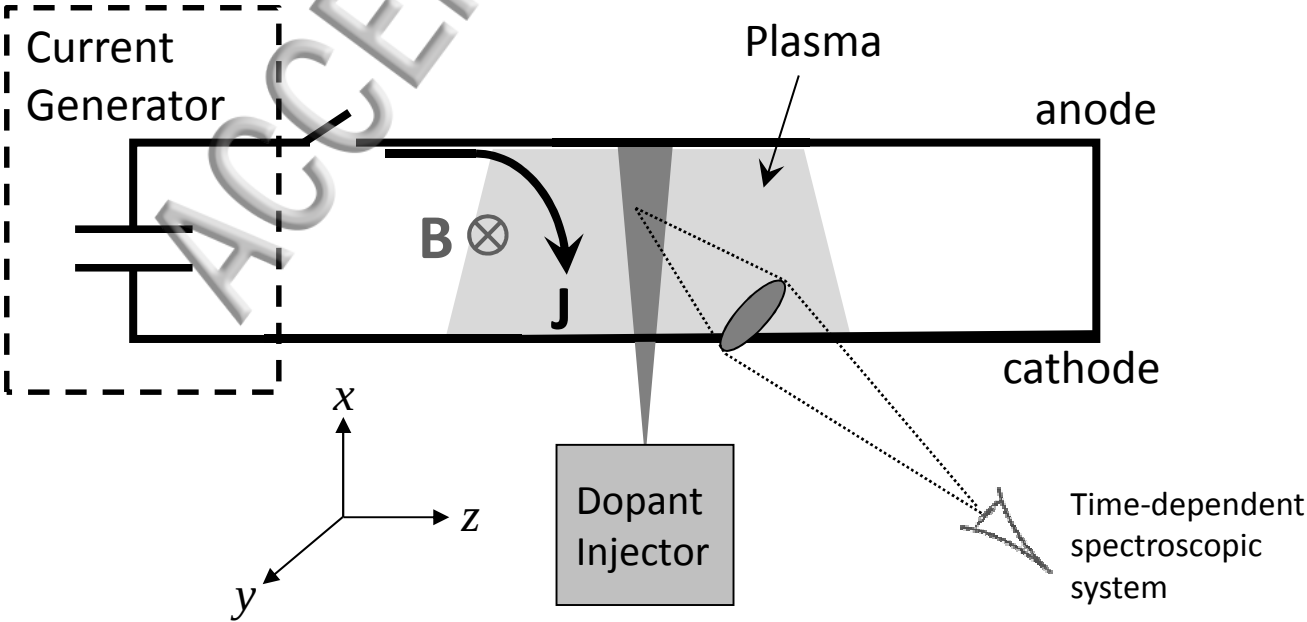
Current
Generator
Plasma
anode
B
J
cathode
x
z
y
Dopant
Injector
Time-dependent
spectroscopic
system

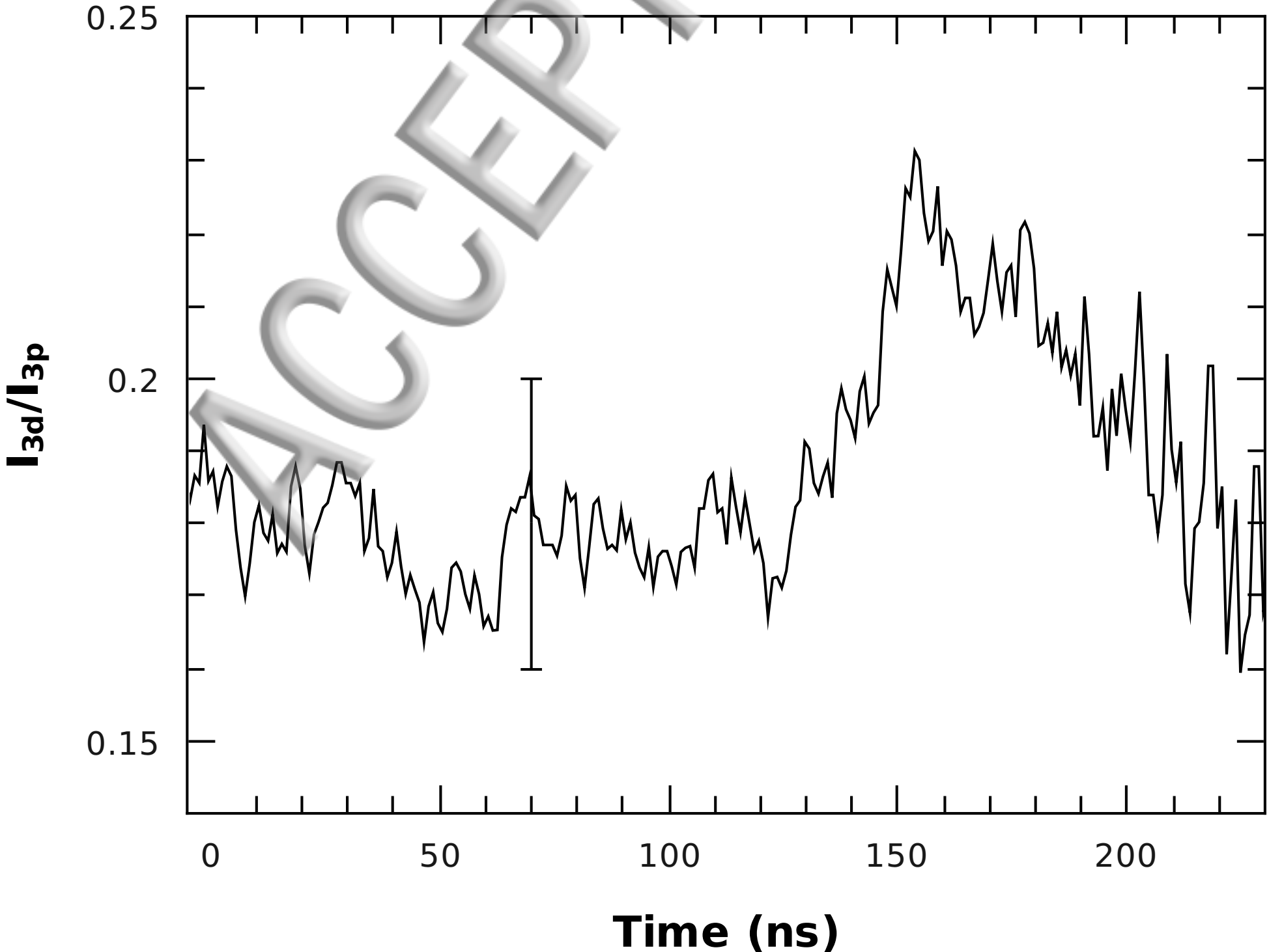

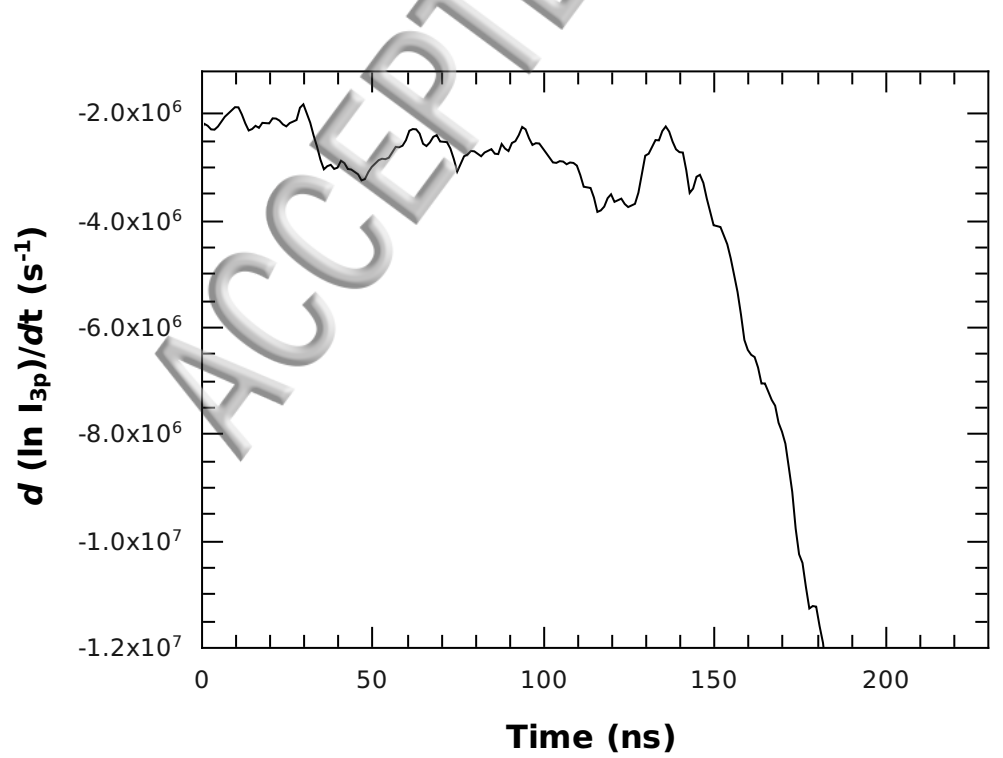
-2.0x10^6
-4.0x10^6
-6.0x10^6
-8.0x10^6
-1.0x10^7
-1.2x10^7
d (ln I3p)/dt (s-1)
0
50
100
150
200
Time (ns)

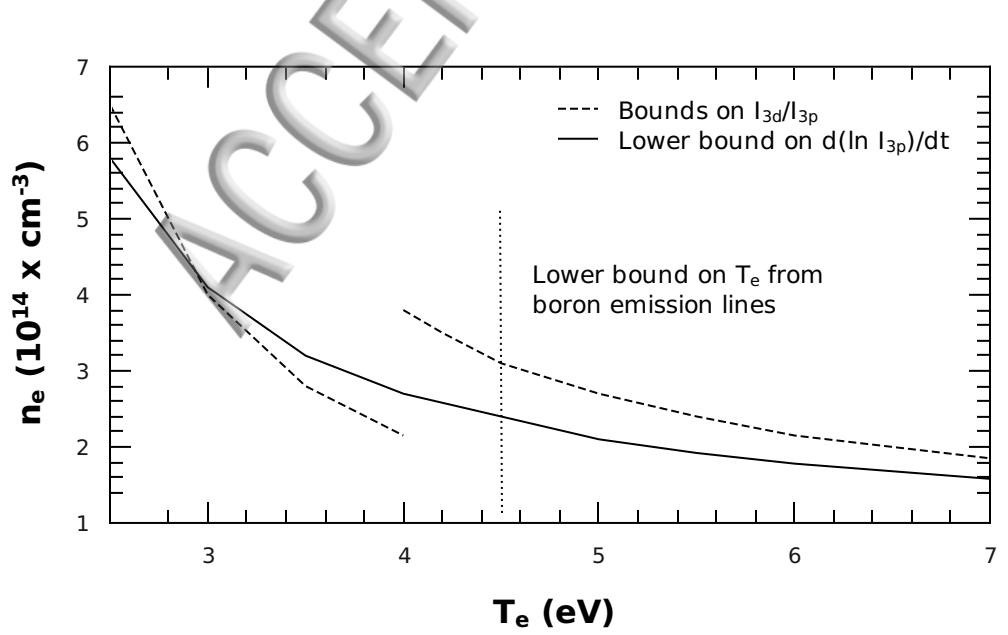
Bounds on I_{3d}/I_{3p}
Lower bound on $d(\ln I_{3p})/dt$
Lower bound on T_e from boron emission lines
n_e (10^{14} x cm^{-3})
T_e (eV)
1
2
3
4
5
6
7